ARTICLE

$MAPbBr_{3-n}X_n$ (X=Cl, I) Single Crystal Narrowband Photodetectors for Potential Application in Traffic Light Recognition

Feng-Xia Liang, [a] Shi-Fu Li, [b] Jie Yu, [b] Liang-Liang Zhou, [b] Jiang Wang, [a] Can Fu, [a] Xiang An, [ac] Jian-An Huang, [c] Li Wang, * [a] Lin-Bao Luo * [a]

Received 00th January 20xx,
Accepted 00th January 20xx

DOI: xx.xxxx/x0xx00000x

Narrowband photodetection system that can specifically distinguish green, yellow and red light has potential application in intelligent transportation system. In this work, a series of $MAPbBr_{3-n}X_n$ (X=Cl, I) single crystal films with controllable thickness have been grown through space-limited inverse temperature crystallization. Filter-free narrowband photodetectors with peak responses at 505, 590 and 620 nm, corresponding to the green, yellow and red traffic light, are successfully achieved through the charge collection narrowing mechanism. The as-fabricated narrowband photodetectors demonstrate superior performance, with the full-width at half-maximum all less than 35 nm, and a maximum responsivity of 182 mA/W, and specific detectivity of $9.68*10^{10}$ Jones respectively. Finally, a traffic light recognition assembly based on the three narrowband photodetectors is constructed. The photocurrent of the photodetector is approximately five to ten times that of the interference from other light sources, indicating the good color recognition capability for the traffic lights.

Introduction

In the application fields of image sensing, color recognition, artificial vision and biomedicine, there exists great demands for narrowband photodetectors that could recognize a tiny spectral range while other wavelengths do not respond.[1-5] Conventionally, the state-of-the-art commercial spectrum-selective photodetection system, for instance, charge-coupled device imaging relies on the combination of broadband photodetector with optical filters.[6-8] However, these optical filters not only hinder the development of miniaturization and integration of devices, but also add the complexity and cost of device manufacturing.[7, 9] Meanwhile, most available commercial optical filters could not always satisfy the needs for the various applications, and the full-width at half-maximum (FWHM) is also restricted to approximately 40-80 nm.[2]

In view of this, filter-free narrowband photodetectors based on alternative routes are studied to circumvent the drawbacks of optical filters. For instance, narrowband photodetection could be realized by using photoactive materials with narrowband absorption properties,[10-12] and the absorption enhancement of a particular wavelength range via plasmon resonance.[13] Besides, researchers have recently developed a novel mechanism to achieve narrowband detection through narrowing the charge collection efficiency to the desired spectrum region (charge collection narrowing, CCN).[14] Perovskite emerged as the most potential material to realize the filter-free narrowband photodetector through such CCN concept, due to their outstanding carrier transport properties, tunable optical bandgaps and low-cost solution preparation processes.[15-17] Among the great variety of perovskites, the organic-inorganic mixed-halide perovskites are designed via halide exchanging and the absorption edge could be continuously tuned over a large wavelengths range, which is particularly attractive for the different narrowband application scenarios.[9, 18] On the other hand, perovskite single crystals show much more promising potential in photoelectric devices than their polycrystalline films, due to the improved properties of higher carrier mobility, longer carrier lifetime and diffusion length.[19-21] Although large sized-bulk mixed-halide perovskite single crystal with millimeter or centimeter thickness is prepared, it is still challenging to slice or deposit electrode on the fragile crystals.[22] Moreover, the macroscopic large-sized single crystals could not be synthesized on planar substrates, which hinders the further device integration. In this regard, the thickness controllable crystal film appears highly intriguing to make efficient optoelectronic devices. However, as far as we know, there exists little reports on the fabrication of narrowband photodetectors employing mixed-halide perovskite crystal films, which may be ascribed to the difficulty in acquiring large and high-quality crystal films.

In this work, we here designed a series of novel narrowband photodetectors based on $MAPbBr_{3-n}X_n$ single crystal films synthesized via a modified space-confined inverse temperature crystallization,[23, 24] and further applied it to the identification of different color LEDs employed in the traffic lights. In order to realize the CCN mechanism, the photodetectors were designed intentionally with light illumination and Au electrodes at two

[a] School of Microelectronics, Hefei University of Technology, Hefei, Anhui 230009, P. R. China
E-mail: wlhgd@hfut.edu.cn(L.Wang), luolb@hfut.edu.cn(L.B.Luo).
[b] School of Materials Science and Engineering, Hefei University of Technology, Hefei, Anhui 230009, P. R. China
[c] Faculty of Medicine, Faculty of Biochemistry and Molecular Medicine, University of Oulu, Oulu 90220, P. R. Finland
Electronic Supplementary Information (ESI) available: [Fig. S1-S8]. See DOI: xx.xxxx/x0xx00000x

opposite sides of the as-synthesized crystal film, the light illuminated from the front surface while the electrodes deposited at the bottom. Three different narrowband photodetectors with peak responses at 505, 590 and 620 nm are successfully tuned, with a FWHM of less than 35 nm. At last, a sample assembly with excellent color recognition for traffic lights was constructed employing the as-obtained narrowband photodetector. Each photodetector mainly responds to the corresponding LED lamp, with less interference from other LED lamps. These results may have potential applications in the intelligent vehicles and automatic driving systems.

Results and discussion

Fig. 1a shows the schematic illustration of a $MAPbBr_{3-n}X_n$ single crystal photodetector, which is mainly composed of glass substrate, perovskite single crystal film and gold electrode. The perovskite single crystal films were grown by the reported space-limited inverse temperature crystallization method,[23] the flow chart of which was drawn in Fig. S1. Briefly, perovskite precursor solution was injected into the limited space formed between two glass substrates and the interlayer U-type polytetrafluoroethylene (PTFE) film, which could hinder the lateral growth of the perovskite. Through further tuning the thickness of the PTFE film, the perovskite crystal with different thickness could be easily realized. To fabricate the $MAPbBr_{3-n}X_n$-based photodetector, two 50-nm-thick Au electrodes were deposited onto the crystal films employing a homemade shadow mask through an e-beam evaporator. Noted that here the incident light is illuminated from the side without the electrode of the photodetector. In such a particular design, the photogenerated carriers that could be collected by the bottom electrode are jointly decided by the photon distribution, carrier diffusion length and electric field distribution, as exhibited in Fig. 1b. The photon distribution varies greatly with the incident light wavelength according to the strongly wavelength dependent absorption coefficient.[25-27] To be specific, the incident light with short wavelength (green arrow) is intensively absorbed at the top surface of the film due to its relatively higher absorption coefficient. While for the long incident light (yellow arrow), it penetrates deeper into the film due to the gradually decreased absorption coefficient. For the photons with energy lower than the bandgap (red arrow), it simply passes through the device as the absorption is neglectable. Followingly, the photogenerated carriers may go through a diffusion process before being collected by the electric field generated by the bottom gold electrode. It is apparent that less photogenerated carriers could be collected for the short wavelength, as a result of the presence of defects on the crystal surface,[28, 29] a relatively lower light penetration depth and longer distance in the transport process. Meanwhile, the photogenerated carriers near the bandgap are more likely to diffuse to the electric field area due to the greatly increased penetration depth. Based on the above discussion, the carrier collection efficiency could be manipulated, and a narrowband spectral response with peak value near the bandgap of perovskite crystals may be achieved, through adjusting the thickness of the perovskite film.

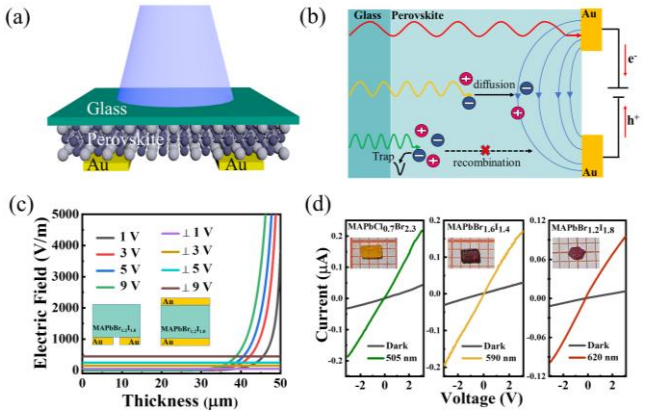

Fig. 1. (a) Schematic illustration of the $MAPbBr_{3-n}X_n$ single crystal narrowband photodetector. (b) The operational mechanism of the narrowband photodetector. (c) Simulation of the distribution of the electric field of the photodetector with vertical electrode or planar electrode under different bias voltages. (d) *I–V* characteristic of devices in the dark and illuminated with 505, 590 and 620 nm, respectively. The inset shows the photograph of $MAPbBr_{3-n}X_n$ crystal films.

On the other hand, the devices with vertical electrode has also been investigated to exhibit narrowband characteristics, usually at the relatively low voltage (e.g., 1-2 V).[3, 23] In order to verify the advantages of planar electrode structure, Silvaco TCAD was employed to simulate the electric field distribution of the photodetector with the vertical and planar bottom electrode structure respectively under different bias voltage from 1-9 V, as shown in Fig. 1c. The optical constants of the materials were extracted from the previous literature.[25] It is noticed that the electric field in a planar electrode structure is mainly distributed within 10 μm from the bottom electrode, while its counterpart of the vertical electrode penetrates longitudinally through the whole crystal film. In view of this, photodetectors with the adopted planar electrode at the bottom may be more superior in maintaining the properties of narrowband spectral response especially under a high working bias.[2, 30]

Next, the morphology and element distribution of the as-synthesized perovskite film were firstly characterized. The inset of Fig. 1d displays a digital photograph of $MAPbBr_{3-n}X_n$ single crystal film with a regular shape and different colors, the color changes from yellow ($MAPbCl_{0.7}Br_{2.3}$) to kermesinus ($MAPbBr_{1.6}I_{1.4}$, $MAPbBr_{1.2}I_{1.8}$) while the shape from tetragonal to hexagonal. Such different shapes are commonly caused by intrinsic crystallographic structures and preferred growth directions.[19] Fig. S2(a-c) presents the cross-sectional SEM images of the crystal films prepared by using 200 μm PTFE. It could be observed that the film exhibits a controllable thickness, with the relative error less than 3%. The EDS mapping patterns in Fig. S3 reveal a homogeneous distribution of C, N, Pb and halogens at a scale of 10 μm. The AFM characterization in Fig. S4 shows the relatively low surface roughness of $MAPbBr_{3-n}X_n$ crystals, with the arithmetic mean roughness (Ra) and root mean square roughness (Rq) less than 51.2 and 64.4 nm, respectively. Finally, the SEM characterization of the device surface in Fig. S2(d) shows that the channel width is about 50 μm. To explore the electrical properties of $MAPbBr_{3-n}X_n$ single crystal

photodetectors, the *I-V* curves of the devices were tested in the dark and with light illumination at 505, 590 and 620 nm, as shown in Fig. 1d. The linear relationship of *I-V* curve indicates that the as-constructed $MAPbBr_{3-n}X_n$ single crystal photodetectors exhibit a typical photoconductor characteristic.

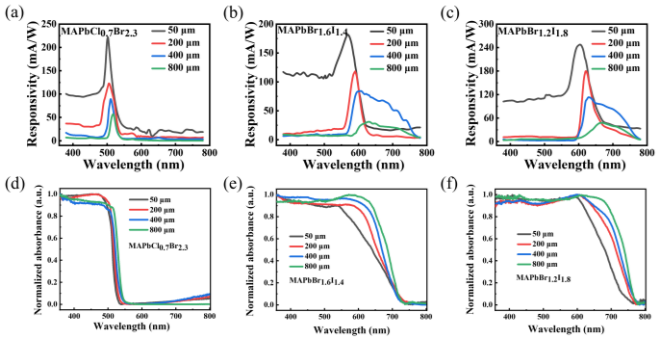

Fig. 2. (a-c) Responsivity spectra of $MAPbCl_{0.7}Br_{2.3}$, $MAPbBr_{1.6}I_{1.4}$ and $MAPbBr_{1.2}I_{1.8}$ narrowband photodetector under different thickness. (d-f) Normalized optical absorption spectrum of $MAPbCl_{0.7}Br_{2.3}$, $MAPbBr_{1.6}I_{1.4}$ and $MAPbBr_{1.2}I_{1.8}$ narrowband photodetector under different thickness.

As the thickness of the perovskite crystal film is a critical parameter for the realization of the CCN mechanism, the spectral response of the photodetector with different crystal thickness was measured and displayed in Fig. 2a-c, at a bias of 5 V. Noted that the responsivity (*R*) is calculated using the following equation:[31]

$$R = (I_p - I_d)/(P_\lambda * S) \quad (1)$$

where $\boldsymbol{I_P}$, $\boldsymbol{I_d}$, $\boldsymbol{P_\lambda}$ and $\boldsymbol{S}$ represent the photocurrent, the dark current, irradiation power and the effective illuminated area, respectively. Fig. 2a-c compares the calculated responsivity of the three $MAPbBr_{3-n}X_n$ single crystal photodetector with thickness varied from 50 to 800 μm. With the increase of film thickness, it is found that the short wavelength photogenerated carriers are more greatly suppressed as it is supposed, and an apparent narrowband spectral near the absorption edge gradually appeared for $MAPbCl_{0.7}Br_{2.3}$ single crystal (Fig. 2a and Fig. 2d). For instance, at the thickness of 200 μm, a peak responsivity of 124.5 mA/W at 505 nm is exhibited, and the FWHM is less than 35 nm. Further careful examination found that the response peak slightly shifted to the longer wavelength, which is quite in accordance with the reported work.[23, 32] The origin of such shift has been attributed to the rapidly decreasing absorption coefficient near the absorption edge, and thus the corresponding absorption in the relatively longer wavelength would be greatly increased with the increase of thickness. Such assumption is confirmed by the measured optical absorption of $MAPbCl_{0.7}Br_{2.3}$ with different thicknesses in Fig. 2d. On the contrary, the $MAPbBr_{1.6}I_{1.4}$ and $MAPbBr_{1.2}I_{1.8}$ single crystal photodetectors show distinctly different spectral response characteristics (Fig. 2b-c). Noted that the latter two devices exhibit good narrowband response characteristics at about 590 and 620 nm, with the FWHM all less than 35 nm at the thickness of 200 μm. Nevertheless, an apparent broad spectral response with FWHM larger than 100 nm appeared with the thickness increased to 400 or 800 μm. Such abnormal response has been attributed to the quite different absorption characteristics of the $MAPbBr_{3-n}I_n$ crystal drew in Fig. 2e and 2f, which exhibit an apparent slowly descending absorption edge in comparison with $MAPbBr_{0.7}Cl_{2.3}$.[33, 34] Specifically, for 200 μm $MAPbBr_{3-n}I_n$, it is found that there exists a big discrepancy between absorption and the spectral response. Similar to the short wavelength region, the response of the relatively longer wavelength region (e.g., >590 nm for $MAPbBr_{1.6}I_{1.4}$ and >620 nm for $MAPbBr_{1.2}I_{1.8}$) is also much more greatly suppressed. We may attribute such interesting result to the more compounded longer wavelength generated carriers by the defects in bulk or at the bottom, during the complex photoelectric conversion process. For 400-800 μm film, the optical absorption may play a significant role here and the corresponding spectral response of the above mentioned long band gradually strengthens, due to the significantly increased absorption with the increase of thickness[34]. In light of this, a much broader FWHW gradually emerges with the increase of thickness to 400 or 800 μm for $MAPbBr_{3-n}I_n$ devices. To be concluded, the photogenerated charges appear within the perovskite film upon light irradiation and the recombination occurs simultaneously in bulk and all interfaces. Eventually, the uncompounded carriers could be collected by the bottom Au electrodes in our design (Fig. 1a) and the photocurrent is generated. The final spectral response is decided by the competition between the light absorption and recombination.

To verify that the spectral response of the device is related to the position of the light illumination. The response spectra of the devices (200 μm thickness) with light illumination and gold electrodes on the same side were measured for comparison. As shown in the Fig. S5, the $MAPbBr_{3-n}X_n$ (X=Cl, I) photodetectors exhibit an apparent broad spectral response, which is quite in accordance with the theoretical analysis. It should be noted that such broad-spectrum response has larger responsivity than the as-fabricated narrowband detector. For example, the $MAPbCl_{0.7}Br_{2.3}$, $MAPbBr_{1.6}I_{1.4}$ and $MAPbBr_{1.2}I_{1.8}$ based devices achieved peak responses of 763.5, 736.2 and 801.1 mA/W at 498, 585 and 625 nm respectively. It is reasonable as more absorbed light generated carriers could be collected with the illumination light and electrode on the same side.

Based on the above results, narrowband $MAPbBr_{3-n}X_n$ single crystal photodetectors with a thickness of 200 μm were chosen for the traffic light application, with peak responses at 505, 590 and 620 nm, and FWHM less than 35 nm (see the Fig. 3a). Such spectral response is in accordance with the luminous ranges of green (500-510 nm), yellow (585-595 nm) and red (620-630 nm) signals in the national standard of the People's Republic of China-road traffic signal lamps. For narrowband photodetectors, the sensitivity plays a significant role in the actual application scenarios and is firstly evaluated through a series of photoelectric tests. Fig. 3b summarized the relative balance $(V_{max} - V_{min})/V_{max}$ as a function of the modulating frequency of the $MAPbCl_{0.7}Br_{2.3}$, $MAPbBr_{1.6}I_{1.4}$ and $MAPbBr_{1.2}I_{1.8}$ based narrowband photodetectors. The −3dB frequency (f_{-3dB}: defined as the frequency where the photoresponse declined to 70.7% of its maximum value)[35] could reach 835, 840 and 1410 Hz, respectively. Based on their definitions,[36] the rise/fall time was estimated from the magnified photoresponse curve recorded at 835, 840 and 1410 Hz (see the Fig. 3c), which were calculated to be 261.24/440.51, 360.45/415.31 and 194.6/262.47 μs,

respectively. Fig. 3d shows the photocurrent response of $MAPbBr_{3-n}X_n$ single crystal photodetectors under various light intensities of the 505, 590 and 620 nm monochromatic light, from which a linear dynamic range (LDR)[37] of 32, 41 and 48 dB were achieved, respectively. It is noted that the LDR does not reach its maximum value due to the limited power density of the light source in the lab. As exhibited in Fig. S6(a), the dependence of photocurrent on light intensity was further fitted with the widely employed power law $I_{ph} \sim P^{\theta}$, where I_{ph} is defined as the net photocurrent ($I_{ph} = I_{light} - I_{dark}$) and θ is an empirical value[38]. The θ value of approximately 0.63, 0.74 and 0.81 were acquired for $MAPbCl_{0.7}Br_{2.3}$, $MAPbBr_{1.6}I_{1.4}$ and $MAPbBr_{1.2}I_{1.8}$ respectively, the deviation of which from the ideal value (θ=1) indicated the existence of recombination loss in the device. Moreover, the *R* and external quantum efficiency (*EQE*) are also light intensity dependent. Noted that the *EQE* is calculated using the following equation:[39]

$$EQE = (hcR)/(e * \lambda) \quad (2)$$

where ***h*** is Planck constant, ***c***, ***e***, and ***λ*** represent the speed of light, elementary electrical charge, and wavelength, respectively. Fig. S6(b-d) shows the obtained *R* and *EQE* with the increase of light intensity, both of which decrease as the light intensity increase. This can be attributed to the higher recombination loss upon light irradiation with higher intensity because more carriers are generated.[40] Besides the light intensity, the impact of applied bias on the performance of the narrowband photodetector was also measured. Fig. S7 compares the *EQE* of the $MAPbBr_{3-n}X_n$ single crystal narrowband photodetectors (200 μm) at an external bias of 1, 3, 5 and 9 V, respectively. It could be clearly observed that the *EQE* of the narrowband photodetectors rises apparently, while the narrowband properties remain nearly unchanged with the increase of the voltage. At the bias of 9 V, the maximum EQE of the as-fabricated three narrowband photodetectors could reach a more competitive value of 49.9%, 43.1% and 50.3%, respectively.

In addition, the specific detectivity (*D**) was investigated. *D** represents the detection limit of a photodetector, and can be determined through the following equations:[31]

$$D^* = (S\Delta f)^{1/2}/NEP \quad (3)$$

$$NEP = (\overline{i_n^2}^{1/2})/R \quad (4)$$

where Δf is the bandwidth, $\overline{i_n^2}^{1/2}$ is the root-mean-square value of the noise current, and NEP is the noise equivalent power. The noise spectral densities of the three narrowband photodetectors at 1 Hz bandwidth were extracted to be $3.84*10^{-12}$, $1.7*10^{-12}$ and $2.22*10^{-13}$ $AHz^{-1/2}$ from the fast Fourier transform (FFT) of the dark current, as shown in Fig. 3e, respectively. According to the above formula, the maximum specific detectivity were deduced to be $4.06*10^{9}$ for $MAPbCl_{0.7}Br_{2.3}$, $1.10*10^{10}$ for $MAPbBr_{1.6}I_{1.4}$ and $9.68*10^{10}$ Jones for $MAPbBr_{1.2}I_{1.8}$, as shown in Fig. 3f. Table S1 summarizes the key performance figure-of-merits of the $MAPbBr_{3-n}X_n$ single crystal narrowband photodetectors and some representative narrowband photodetectors in the literature. Apparently, most 3D single crystal perovskite-based narrowband photodetector exhibits narrowband characteristics at a relatively larger thickness than the 2D perovskite or 3D polycrystalline perovskite film. The large conductivity anisotropy along the in-plane and out-of-plane direction of 2D layered perovskite and the short carrier diffusion length of 3D perovskite polycrystalline films, which usually compound short wavelength photogenerated carriers relatively quickly, is considered as the origin of the thickness difference.[1-3, 41, 42] Nevertheless, the as-fabricated 3D perovskite single crystal narrowband photodetectors exhibit comparable performances to most of the previously reported CCN based narrowband perovskite photodetectors. At last, the stability of the three devices were measured. Fig. S8 exhibit the temporal photoresponse before and after storage in ambient conditions without any protection for 30 days. Clearly, the photoresponse characteristics were well-preserved with good cycling stability, and the proportion of decline was less than 6%.

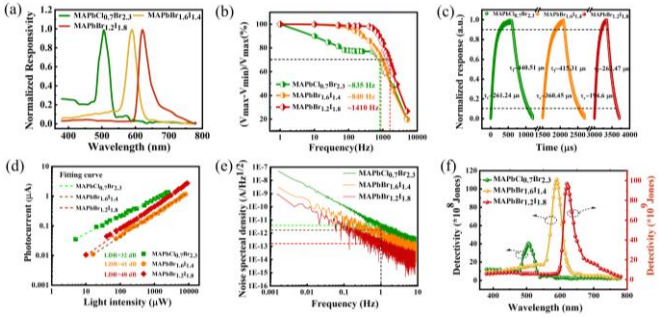

Fig. 3. (a) Normalized responsivity of $MAPbBr_{3-n}X_n$ narrowband photodetector at 200 μm thickness. (b) Relative balance $(V_{max} - V_{min})/V_{max}$ versus switching frequency of 530 nm incident light. (c) Enlarged response curve of devices at 835, 840 and 1410 Hz modulation frequencies respectively, which for estimating the response speed. (d) Power dependent photocurrent of $MAPbBr_{3-n}X_n$ narrowband photodetector. (e) Noise spectral density of $MAPbBr_{3-n}X_n$ narrowband photodetector based on the fast Fourier transform of the dark current. (f) The specific detectivity of $MAPbCl_{0.7}Br_{2.3}$, $MAPbBr_{1.6}I_{1.4}$ and $MAPbBr_{1.2}I_{1.8}$ narrowband photodetector under 5 V bias voltage.

To further investigate the recognition capability of the as-obtained three narrowband photodetector PD1 (green), PD2 (yellow) and PD3 (red) for the corresponding green, yellow and red LED lamps, a traffic light recognizing assembly was constructed as shown in Fig. 4a. The devices were placed on the PCB board, with the electrode welded to the PCB board with silver wire and solder wire (Fig. 4b). With the help of the mask, each LED lamp illuminates three devices simultaneously and the photocurrent were measured under the illumination of three different LED lamps sequentially. As exhibited in Fig. 4c, each vertical column compares the obtained current values of the three different devices under the same LED lamp while each horizontal row shows a comparison of the current values of the same device under three different LED lamps. Apparently, the current values of the devices show a difference of about five to ten times for either each column or row. To be specific, take the first row for example, the current of PD1 under green LED lamp illumination (83.8 nA) is about eight or ten times that of the yellow (10.9 nA) and red (8.8 nA) interference LED lamps, at the same power intensities of 45 μW/cm^2. Such numerical difference in current is sufficient to be distinguished by the circuit system and make it possible for the identification of the traffic light. Fig. 4d further compares the normalized photocurrent of each device

under different LED lighting conditions, which present the similar results as Fig. 4c and little interference is observed by the other two types of LED lamps.

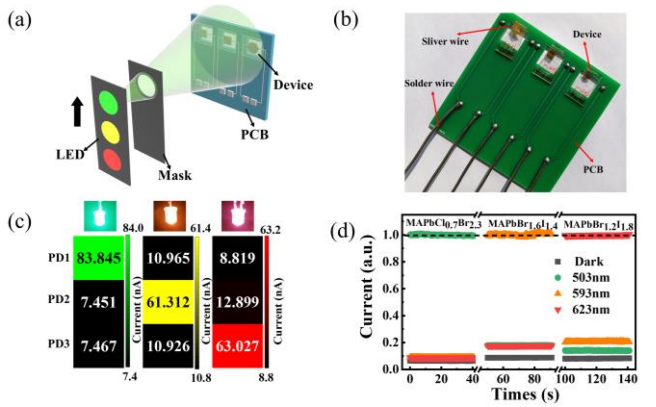

Fig. 4. (a) Schematic illustration of the traffic light recognizing assembly. (b) The photograph of the traffic light recognizing assembly. (c) Photocurrent data of the traffic light recognizing assembly under green, yellow, and red LED illumination. (d) The percentage of the current of the device under different illumination conditions relative to the average photocurrent of the operating wavelength.

Conclusions

In summary, a series of $MAPbBr_{3-n}X_n$ (X=Cl, I) single crystal films with controllable thickness have been synthesized. Through constructing a simple planar structure device, three narrowband perovskite single crystal photodetectors were successfully achieved, with peak response at 505, 590 and 620 nm respectively, all have a FWHM of less than 35 nm, a maximum -3 dB bandwidth of 1410 HZ. The performance of the as-fabricated $MAPbBr_{3-n}X_n$ single crystal narrowband photodetector is comparable to most of the narrowband photodetector reported previously. Lastly, $MAPbBr_{3-n}X_n$ single crystal narrowband photodetectors were assembled for traffic light recognition, which showed good capability in recognition of red, yellow, and green LEDs employed in the traffic lights. The as-fabricated narrowband photodetection system has great potential in the future for intelligent vehicle and driverless systems applications.

Experimental

Materials Synthesis: $MAPbBr_{3-n}X_n$ single crystal thin films were prepared by the previously reported space-limited inverse temperature crystallization method. First, different types of precursor solution were prepared. For $MAPbCl_{0.7}Br_{2.3}$, 0.693 mmol MACl and $PbCl_2$, 2.307 mmol MABr and $PbBr_2$ were dissolved in 1.65 mL of N, N-dimethylformamide (DMF, >99.9%) and 0.35 mL of dimethyl sulfoxide (DMSO, >99.9%) mixed solution. For $MAPbBr_{1.6}I_{1.4}$, 1.596 mmol MABr and $PbBr_2$, 1.404 mmol MAI and PbI_2 were dissolved in 1 mL of DMF and 2 mL of γ-butyrolactone (GBL, >99.9%) mixed solution. For $MAPbBr_{1.2}I_{1.8}$, 1.211 mmol MABr and $PbBr_2$, 1.789 mmol MAI and PbI_2 were dissolved in 1 mL of DMF and 3 mL of GBL mixed solution. All the precursor solutions were stirred for 2 h at 40 ℃ and then passed through a needle filter. Next, a limited space is structured by clipping two glass substrates and a U-style thin polytetrafluoroethylene (PTFE), with PTFE in the middle. Noted that before assembly, the PTFE and glass substrate were cleaned with deionized water, alcohol, and acetone sequentially via ultrasonic process. One of the glass substrates was performed hydrophilic treatment with an oxygen plasma cleaner for 10 min. Then, the perovskite precursor solution was injected into the as-formed limited space and the whole unit was placed in the drying cabinet. For the synthesis of thin film of $MAPbCl_{0.7}Br_{2.3}$, the temperature was set to be 50 ℃ for 24 h, while 60 ℃ for 48 h for $MAPbBr_{1.6}I_{1.4}$ and $MAPbBr_{1.2}I_{1.8}$. And then, the perovskite thin film formed on the hydrophilic glass substrate. Finally, the as-synthesized single crystals were cleaned with chlorobenzene (C_6H_5Cl, Sinopharm, ⩾ 99.5%) for about 2 min to remove the residual precursor solution at the film surface, and then fully dried in a vacuum drying oven.

Device Fabrication, Characterization and Theoretical Simulation: To fabricate the $MAPbBr_{3-n}X_n$ based photodetectors, a pair of Au electrodes (50 nm) with the channel width of 50 μm were deposited by electron beam evaporation, with the help of a lab-built shadow mask. At the front surface, the single crystal film is covered with black tape around it, leaving a square illuminated area of approximately 0.01 cm^2. The square area exposed by black tape at the front surface is regarded as the device area. The morphology of the perovskite crystal films was characterized through a field-emission SEM (Hitachi, SU8020). The surface roughness of perovskite crystal films was characterized by atomic force microscopy (AFM, Dimension Icon). Optical absorption of perovskite crystal films was studied with a UV–vis spectrophotometer (UV-2550, Shimadzu, Japan). The optoelectrical measurement was performed on a semiconductor characterization system (Keithley 2400). In order to carry on the spectral response analysis, an Xe lamp (CEL-HXF 300) attached with a monochromator (Zolix Instruments, Omni-nx I) was employed. For response speed study, 530 nm laser diode was powered with a signal generator (Tektronix, TDS2022B) to produce the pulsed light signal with varied frequencies, and an oscilloscope (Tektronix, TDS2012B) was used to record the output electrical signal. The power intensity of all light sources was accurately calibrated by a power meter (Thorlabs GmbH., PM 100D). The LED lamps were obtained from commercial sources, among which green, yellow and red LED have a luminescence range of 500-510, 588-592, and 620-625 nm, respectively. Technology computer aided design (TCAD) software was used to simulate the electric field distribution of the device.

Author Contributions

There are no conflicts to declare.

Acknowledgements

This work was supported by the National Natural Science Foundation of China (NSFC, Nos. 62074048 and 61675062), the Fundamental Research Funds for the Central Universities under Grant PA2020GDKC0014, Grant JZ2022HGQA0185 and Grant JZ2018HGXC0001, the Key Research and Development Plan of Anhui Province under Grant 2022f04020007, the Key Project of Natural Science Research in Universities of Anhui Province under Grant KJ2020A0536, and the Postgraduate Academic Innovation Project of Anhui Province under Grant 2022xscx014.

Notes and references

1. J. Xue, Z. Zhu, X. Xu, Y. Gu, S. Wang, L. Xu, Y. Zou, J. Song, H. Zeng and Q. Chen, *Nano Lett.*, 2018, **18**, 7628-7634.
2. P. Zhang, Y. Hua, X. Li, L. Zhang, L. Liu, R. Li, G. Zhang and X. Tao, *J. Mater. Chem. C*, 2021, **9**, 2840-2847.
3. Y. Fang, Q. Dong, Y. Shao, Y. Yuan and J. Huang, *Nat. Photonics*, 2015, **9**, 679.
4. L. Li, S. Ye, J. Qu, F. Zhou, J. Song and G. Shen, *Small*, 2021, **17**, 2005606.
5. J. Miao and F. Zhang, *J. Mater. Chem. C*, 2019, **7**, 1741-1791.
6. A. Hijazi, A. Friedl, C. Cierpka, C. Kaehler and V. Madhavan, *Meas. Sci. Technol.*, 2017, **28**, 115401.
7. R. D. Jansen-van Vuuren, A. Armin, A. K. Pandey, P. L. Burn and P. Meredith, *Adv. Mater.*, 2016, **28**, 4766-4802.
8. R. Lukac, *J. Real-Time Image Process.*, 2006, **1**, 45-52.
9. Q. Lin, A. Armin, P. L. Burn and P. Meredith, *Nat. Photonics*, 2015, **9**, 687.
10. S. Yoon, Y.-H. Ha, S.-K. Kwon, Y.-H. Kim and D. S. Chung, *Acs Photonics*, 2018, **5**, 636-641.
11. D. M. Lyons, A. Armin, M. Stolterfoht, R. C. R. Nagiri, R. D. Jansen-van Vuuren, B. N. Pal, P. L. Burn, S.-C. Lo and P. Meredith, *Org. Electron.*, 2014, **15**, 2903-2911.
12. S.-J. Lim, D.-S. Leem, K.-B. Park, K.-S. Kim, S. Sul, K. Na, G. H. Lee, C.-J. Heo, K.-H. Lee, X. Bulliard, R.-I. Satoh, T. Yagi, T. Ro, D. Im, J. Jung, M. Lee, T.-Y. Lee, M. G. Han, Y. WanJin and S. Lee, *Sci. Rep.*, 2015, **5**, 7708.
13. A. Sobhani, M. W. Knight, Y. Wang, B. Zheng, N. S. King, L. V. Brown, Z. Fang, P. Nordlander and N. J. Halas, *Nat. Commun.*, 2013, **4**, 1643.
14. A. Armin, R. D. Jansen-van Vuuren, N. Kopidakis, P. L. Burn and P. Meredith, *Nat. Commun.*, 2015, **6**, 6343.
15. J. Wang, S. Xiao, W. Qian, K. Zhang, J. Yu, X. Xu, G. Wang, S. Zheng and S. Yang, *Adv. Mater.*, 2021, **33**, 2005557.
16. Y. Hou, C. Wu, X. Huang, D. Yang, T. Ye, J. Yoon, R. Sriramdas, K. Wang and S. Priya, *Adv. Funct. Mater.*, 2021, **31**, 2007016.
17. J. Zhou, J. Luo, X. Rong, P. Wei, M. S. Molokeev, Y. Huang, J. Zhao, Q. Liu, X. Zhang, J. Tang and Z. Xia, *Adv. Opt. Mater.*, 2019, **7**, 1900139.
18. W. Wu, X. Wang, X. Han, Z. Yang, G. Gao, Y. Zhang, J. Hu, Y. Tan, A. Pan and C. Pan, *Adv. Mater.*, 2019, **31**, 1805913.
19. Y. Liu, Z. Yang, D. Cui, X. Ren, J. Sun, X. Liu, J. Zhang, Q. Wei, H. Fan, F. Yu, X. Zhang, C. Zhao and S. Liu, *Adv. Mater.*, 2015, **27**, 5176-5183.
20. A. A. Zhumekenov, M. I. Saidaminov, M. A. Haque, E. Alarousu, S. P. Sarmah, B. Murali, I. Dursun, X.-H. Miao, A. L. Abdelhady, T. Wu, O. F. Mohammed and O. M. Bakr, *ACS Energy Lett.*, 2016, **1**, 32-37.
21. D. Shi, V. Adinolfi, R. Comin, M. Yuan, E. Alarousu, A. Buin, Y. Chen, S. Hoogland, A. Rothenberger, K. Katsiev, Y. Losovyj, X. Zhang, P. A. Dowben, O. F. Mohammed, E. H. Sargent and O. M. Bakr, *Science*, 2015, **347**, 519-522.
22. M. I. Saidaminov, A. L. Abdelhady, B. Murali, E. Alarousu, V. M. Burlakov, W. Peng, I. Dursun, L. Wang, Y. He, G. Maculan, A. Goriely, T. Wu, O. F. Mohammed and O. M. Bakr, *Nat. Commun.*, 2015, **6**, 7586.
23. H.-S. Rao, W.-G. Li, B.-X. Chen, D.-B. Kuang and C.-Y. Su, *Adv. Mater.*, 2017, **29**, 1602639.
24. Y.-X. Chen, Q.-Q. Ge, Y. Shi, J. Liu, D.-J. Xue, J.-Y. Ma, J. Ding, H.-J. Yang, J.-S. Hu and L.-J. Wan, *J. Am. Chem. Soc.*, 2016, **138**, 16196-16199.
25. P. F. Ndione, Z. Li and K. Zhu, *J. Mater. Chem. C*, 2016, **4**, 7775-7782.
26. P. Loeper, M. Stuckelberger, B. Niesen, J. Werner, M. Filipic, S.-J. Moon, J.-H. Yum, M. Topic, S. De Wolf and C. Ballif, *J. Phys. Chem. Lett.*, 2015, **6**, 66-71.
27. J.-S. Park, S. Choi, Y. Yan, Y. Yang, J. M. Luther, S.-H. Wei, P. Parilla and K. Zhu, *J. Phys. Chem. Lett.*, 2015, **6**, 4304-4308.
28. Y. Liu, X. Zheng, Y. Fang, Y. Zhou, Z. Ni, X. Xiao, S. Chen and J. Huang, *Nat. Commun.*, 2021, **12**, 1686.
29. L. Sun, L. Xu, Y. Xiong, P. Wu, G. Xie and B. Hu, *Adv. Electron. Mater.*, 2019, **5**, 1800759.
30. M. I. Saidaminov, M. A. Haque, M. Savoie, A. L. Abdelhady, N. Cho, I. Dursun, U. Buttner, E. Alarousu, T. Wu and O. M. Bakr, *Adv. Mater.*, 2016, **28**, 8144-8149.
31. F.-X. Liang, J.-J. Jiang, Y.-Z. Zhao, Z.-X. Zhang, D. Wu, L.-H. Zeng, Y. H. Tsang and L.-B. Luo, *Adv. Funct. Mater.*, 2020, **30**, 2001033.
32. Z. Chen, Q. Dong, Y. Liu, C. Bao, Y. Fang, Y. Lin, S. Tang, Q. Wang, X. Xiao, Y. Bai, Y. Deng and J. Huang, *Nat. Commun.*, 2017, **8**, 1890.
33. S. Draguta, O. Sharia, S. J. Yoon, M. C. Brennan, Y. V. Morozov, J. M. Manser, P. V. Kamat, W. F. Schneider and M. Kuno, *Nat. Commun.*, 2017, **8**, 148.
34. Y. Tian and I. G. Scheblykin, *J. Phys. Chem. Lett.*, 2015, **6**, 3466-3470.
35. H. Chen, C. Xie, X. Zhong, Y. Liang, W. Yang, C. Wu and L. Luo, *J. Mater. Chem. C*, 2022, **10**, 6025-6035.
36. J. Wang, Y. Xing, F. Wan, C. Fu, C.-H. Xu, F.-X. Liang and L.-B. Luo, *J. Mater. Chem. C*, 2022, **10**, 12929-12946.
37. P. Wangyang, C. Gong, G. Rao, K. Hu, X. Wang, C. Yan, L. Dai, C. Wu and J. Xiong, *Adv. Opt. Mater.*, 2018, **6**, 1701302.
38. C.-Y. Wu, K.-J. Cao, Y.-X. Le, J.-Y. Li, C.-Y. Zhu, L. Wang, Y.-X. Zhou, D. Wu and L.-B. Luo, *J. Phys. Chem. Lett.*, 2022, **13**, 2668-2673.
39. Z.-X. Zhang, C. Li, Y. Lu, X.-W. Tong, F.-X. Liang, X.-Y. Zhao, D. Wu, C. Xie and L.-B. Luo, *J. Phys. Chem. Lett.*, 2019, **10**, 5343-5350.
40. C. Xie, X.-T. Lu, M.-R. Ma, X.-W. Tong, Z.-X. Zhang, L. Wang, C.-Y. Wu, W.-H. Yang and L.-B. Luo, *Adv. Opt. Mater.*, 2019, **7**, 1901257.
41. J. Li, J. Wang, J. Ma, H. Shen, L. Li, X. Duan and D. Li, *Nat. Commun.*, 2019, **10**, 806.
42. L. Li, L. Jin, Y. Zhou, J. Li, J. Ma, S. Wang, W. Li and D. Li, *Adv. Opt. Mater.*, 2019, **7**, 1900988.

